Intrinsically photosensitive retinal ganglion cells evade temporal filtering to encode environmental light intensity

Shai Sabbah[1*], Carin Papendorp[2], Inbar Behrendt[1], Hala Rasras[1], Jesse Cann[1], Megan L. Leyrer[2], Elizabeth Koplas[2], Marjo Beltoja[2], Cameron Etebari[2], Ali Noel Gunesch[2], Luis Carrete[2], Min Tae Kim[2], Gabrielle Manoff[2], Ananya Bhatia-Lin[2], Tiffany Zhao[2], Henry Dowling[2], Kevin L. Briggman[3] and David M. Berson[2*]

[1] Department of Medical Neurobiology, Faculty of Medicine, The Hebrew University of Jerusalem, Jerusalem, 9112102, Israel

[2] Department of Neuroscience, Brown University, Providence, RI, 02912, USA

[3] Center of Advanced European Studies and Research (Caesar), Max Planck Institute, Bonn, 53175, Germany

[*]Corresponding authors

Summary

The retina encodes environmental light intensity to drive innate physiological responses. The synaptic basis of such coding remains obscure. Intrinsically photosensitive retinal ganglion cells (ipRGCs) are the only retinal output neurons stably encoding intensity. They do so even without their melanopsin photopigment, so specializations in their synaptic drive from bipolar cells (BCs) must also contribute. Here, we shed new light on mechanisms responsible for this unique intensity-coding drive. By ultrastructural reconstruction, we show that specific BC types and unusual ribbon synapses carry photoreceptor signals to ipRGCs. By glutamate imaging and electrophysiology, we show that their light responses are unusually persistent. Still, we find that virtually all BCs encode intensity. Intensity coding becomes restricted to ipRGCs primarily because other RGCs filter out steady-state intensity signals postsynaptically. Thus, neural "pinholes" in global, persistent neural "masking" allow intensity signals to be encoded by ipRGCs and sent to specific centers of the visual brain.

Key words

Retina, irradiance, glutamate, connectomics, retinal ganglion cells, bipolar cells

Introduction

While environmental light intensity (irradiance) is a powerful regulator of behavior, modulating the pupil size, synchronizing the circadian clock, and regulating hormones and mood (Baver et al., 2008; Chen et al., 2011; LeGates et al., 2012; Lucas et al., 2003), the neuronal network generating retinal light-intensity encoding has largely been undeciphered. Most retinal output cells – the retinal ganglion cells (RGCs) do not represent intensity faithfully, as light steps affect their activity only briefly while their maintained firing rates are uncorrelated with light intensity (Baden et al., 2016). However, a subset of RGCs, known as intrinsically photosensitive retinal ganglion cells (ipRGCs) do encode irradiance, because they maintain, essentially indefinitely a spike rate that is proportional to light intensity (Wong, 2012). Thus, ipRGCs are the primary and perhaps sole source of light intensity information for the brain (Schmidt and Kofuji, 2009).

The neuronal networks that allow ipRGCs to report ambient light intensity remain mostly obscure. Like other RGCs, ipRGCs receive rod/cone photoreceptor signals through synaptic input from bipolar cells (BCs), but they are unique among RGCs in also responding to light directly through melanopsin phototransduction (Berson et al., 2002; Provencio et al., 2000; Schmidt et al., 2014; Wong, 2012; Wong et al., 2007; Zhao et al., 2014). Both of these excitatory components are sustained and depend on light intensity (Schmidt and Kofuji, 2009). This implies that the BCs that drive ipRGCs must also carry steady-state intensity-encoding signals. However, while some BCs exhibit more sustained responses than others (Baden et al., 2013; DeVries et al., 2006; Franke et al., 2017), it is unclear whether any are specialized to encode the absolute intensity of environmental light. Each of more than a dozen distinct BC types makes glutamatergic ribbon synapses onto distinct sets of RGCs and amacrine cells (ACs) within specific strata of the inner plexiform layer (IPL) (Helmstaedter et al., 2013; Roska and Werblin, 2001; Shekhar et al., 2016). We sought to determine which BC types provide input onto ipRGCs and whether their light-evoked responses make them uniquely suited for reporting light intensity.

Dendritic stratification of ipRGCs provides some clues about which BC types innervate ipRGCs. The six ipRGCs types, M1 through M6, all exhibit sustained ON-polarity responses (Quattrochi et al., 2019; Zhao et al., 2014) and deploy their dendrites in specific layers near the inner or outer margins of the IPL; some stratify in both (Ecker et al., 2010). Several ipRGC types stratify in the inner half of the (ON) IPL sublayer, where relatively sustained ON-BCs terminate (Baden et al.,

2013; Borghuis et al., 2013; Roska and Werblin, 2001; Wu et al., 2000). Other ipRGCs, surprisingly, arborize at the distal margin of the outer (OFF) IPL sublayer, where OFF-BCs terminate. The ipRGCs that stratify there – the M1, M3 and M6 types – are also ON cells. They apparently receive ectopic ribbon contacts from ON-BC axons in the 'accessory ON sublayer' as they descend toward their main axonal terminal arbor in the inner IPL (Dumitrescu et al., 2009; Hoshi et al., 2009). Ribbon contacts on RGCs typically comprise dyad synapses at which the second postsynaptic process is an AC or, less often, another RGC (Dowling, 1968). Some ribbon synapses, however, are atypical, with only a single postsynaptic partner at the ribbon synapse ("monad") (Kim et al., 2012). Monads have been reported to be the dominant ribbon synapse at ectopic (*en passant*) ribbon contacts from ON BCs (Kim et al., 2012). The presence of monad vs. dyad synapses may affect intensity-coding through temporal filtering, by feedback inhibition of BCs or feedforward inhibition of RGCs. The form of ON-BC ectopic synapses in the accessory ON sublayer, as well as their targets and functional properties, remain largely mysterious, so we aimed to probe their morphological and functional properties and significance.

Here, by combining serial electron microscopic (SBEM) reconstruction, glutamate imaging and patch-clamp recording, we characterize synaptic structure and intensity-encoding capacity within the BC-to-ipRGC circuit, and compare these with BC inputs to selected conventional RGCs. In agreement with past studies (Schmidt and Kofuji, 2009), we found that all ipRGCs receive excitatory, sustained, intensity-encoding synaptic input, regardless of the type of BC, the synapse type, or where in the depth of the IPL they occur (Figure S1). Connectomic analysis shows that ipRGCs receive their excitatory drive from a distinctive collection of BCs, mainly from Types 6, 7, 8 and 9, either through terminal dyad synapses or via ectopic monad synapses; only the M6 type receives any OFF BC input. To assess whether BC types that feed ipRGCs are uniquely specialized to transmit light intensity information, we studied the glutamate release at the stratification depths of BC Types 6, 7, 8 and 9 as compared to that at the terminal depths of other BC types across the IPL. We found sustained and intensity-dependent glutamate release in every IPL layer, including terminals of OFF as well as ON BCs. This means that intensity-coding is not primarily due to specialized BC input. Rather, it seems to arise mainly from the **absence** of high-pass postsynaptic filtering that suppresses steady-state intensity responses in most other RGCs. Conceptually, the retinal mechanism of intensity-dependent signaling revealed here may be described as a neural "pinhole" in an otherwise global, persistent neural "masking" of the bipolar

light intensity signal achieved through reduction in RGC spiking inversely proportional to light intensity. The "pinholes" represent an ipRGC-specific absence of this signal reduction, allowing an unmasked light intensity signal to penetrate and be encoded.

Results

Electron-microscopic reconstruction of BCs and ribbon synapses

In a published serial blockface electron microscopic (SBEM) dataset spanning >200 μm of the adult mouse IPL (Ding et al., 2016), we surveyed RGCs for those consistent with ipRGC morphology, reconstructed them using skeletons, then mapped their inputs from ribbon synapses. We reconstructed the BCs providing those inputs, then sorted them into types based on stratification and the tiling mosaics formed by their terminal arbors (Figure S2). We reconstructed nearly 1,000 BCs comprising the 13 known cone BC types, the rod BC, and the GluMI type (Della Santina et al., 2016; Helmstaedter et al., 2013; Wassle et al., 2009). Figure 1A-C shows reconstructions and provide data on type-by-type terminal arbor area and stratification. An additional sparse 'type' actually appears as collaterals of Type 9 axons that fork off the main shaft in the middle of the inner nuclear layer and arborize mainly in the outer IPL (Park et al., 2020) (personal communication, Wei Li, NEI; Supplementary Discussion on cell type identification). For now, we term these Type 9o (outer) while conventional inner-IPL arbors are called Type 9i (inner). Of the 4163 ribbon synapses identified, most were dyads within terminals. The rest (662) were ectopic (*en passant*) synapses within ON-BC axon shafts or collaterals (Figure 1D). The ectopic ribbons were most abundant at the far outer IPL and were almost exclusively monads, targeting a single postsynaptic partner. Virtually all ectopic synapses comprised multiple ribbons (Figure 1E, gray stripes), each surrounded by vesicles (Figure 1E, black aggregates). Figure S3A-B presents examples of ectopic synapses identified on BC Types 6, 7, 8, and 9. The predominant source of ectopic synapses was Type 6, and these had the largest number of ribbons per synapse (Figure 1F,G).

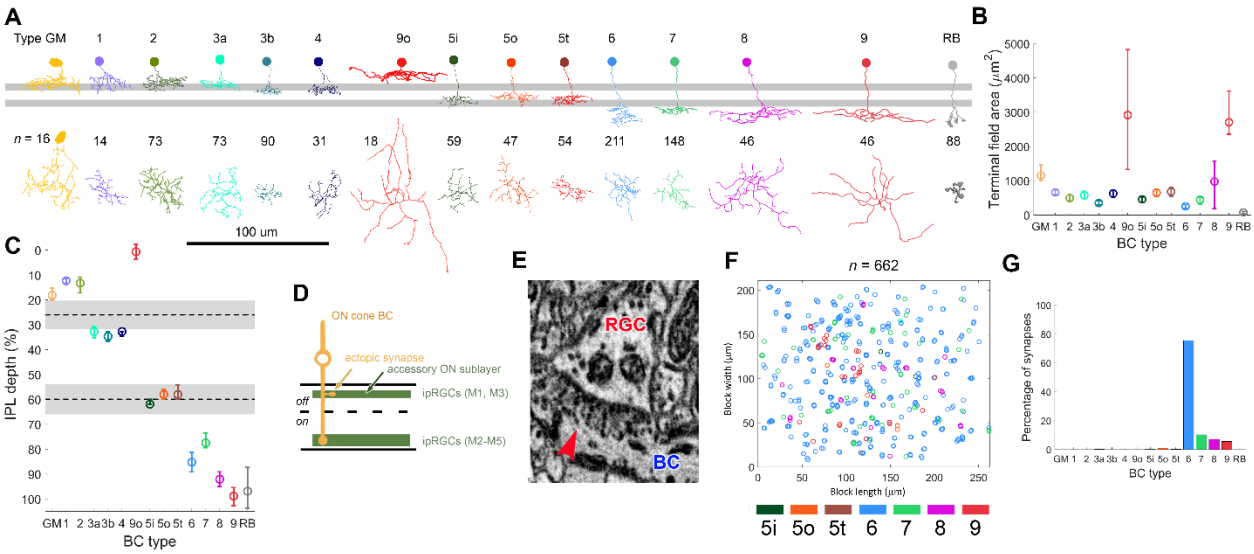

Figure 1. Ectopic synaptic input is ubiquitous in the outer IPL

A. Representatives of the BC types encountered in the SBEM volume, holding the complete BC repertoire in mice and a new outer-IPL arbor of Type 9 BCs (Type 9o). Two horizontal gray stripes mark the ON and OFF cholinergic bands, as estimated from the inner and outer dendritic arbors of ON-OFF-DSGCs (n = 15). **B, C.** Different BC types exhibit characteristic terminal field area (**B**) and stratification depth across the IPL (**C**); dashed lines and shaded gray areas mark the median and first and third quartiles of the cholinergic bands' IPL depth. **D**. A schematic of ectopic ribbon synapse, found at the far outer IPL (IPL depth 5%-25%), from an ON-BC onto the dendrites of ipRGCs. **E**. Example electron micrograph of an ectopic synapse on the shaft of a type 6 BC onto a RGC's dendrite, showing vesicles (black clamps) surrounding 7 ribbons (gray stripes). **F**. Prevalence of ectopic synapses in the SBEM volume by BC type of origin. **G**. Ectopic synapse distribution by BC type. Type 6 BCs are the predominant source of ectopic synapses.

Excitatory input to ipRGCs is derived mainly from bipolar types 6, 7, 8 and 9 through terminal-dyad and ectopic-monad synapses

We identified examples in the volume of five ipRGC types - all but the rare M3 cells (Schmidt and Kofuji, 2011). Cell type assignment was based on statistical comparisons of key morphological features of genetically, morphologically, and physiologically identified ipRGCs (Figure S4). Figure 2 illustrates examples of each ipRGC type along with the locations of their ribbon inputs (red dots in panels A-F; color coded in M-R) and of the bipolar terminal arbors from which they arise (G-L).

The M1 type (Figure 2A,G,M) stratifies in the outer IPL (Figure 2G). There it receives nearly all its ribbon synapses, with very few onto proximal dendrites in the ON sublayer. Most ribbon synapses (>80%) come from Type 6 (Figure 2S), either *en passant* from axon shafts or from short side branches. Nearly all the rest come from Type 9o, another presumed ON BC type. Only a single OFF BC ribbon input was found (Type 2).

Two distinct subtypes shared a resemblance to M2 ipRGCs, called here M2(8) and M2(9). They differed in the balance of inputs from Type 8 and 9 BCs, but also subtly in dendritic stratification and structural affiliation with a widefield AC (Figure S3C,D). M2(8) cells are almost certainly M2 ipRGCs, but it is unclear whether M2(9) cells are M2 ipRGCs or a lookalike type that lacks photosensitivity (see Supplementary Discussion on cell type identification). Collectively, M2(8), M2(9), M4, and M5 ipRGCs stratify exclusively in the inner ON IPL, where they receive their BC input through dyad synapses from axon terminals, mainly Types 6, 7, 8 and 9 (Figure 2B-E, H-K, N-Q, T-W). Among ipRGC types, only the bistratified M6 type received any notable input from OFF-BCs, mainly Type 2 (Figure 2F,L,R,X). A BC-to-ipRGC connectivity matrix is provided in Figure 2Y.

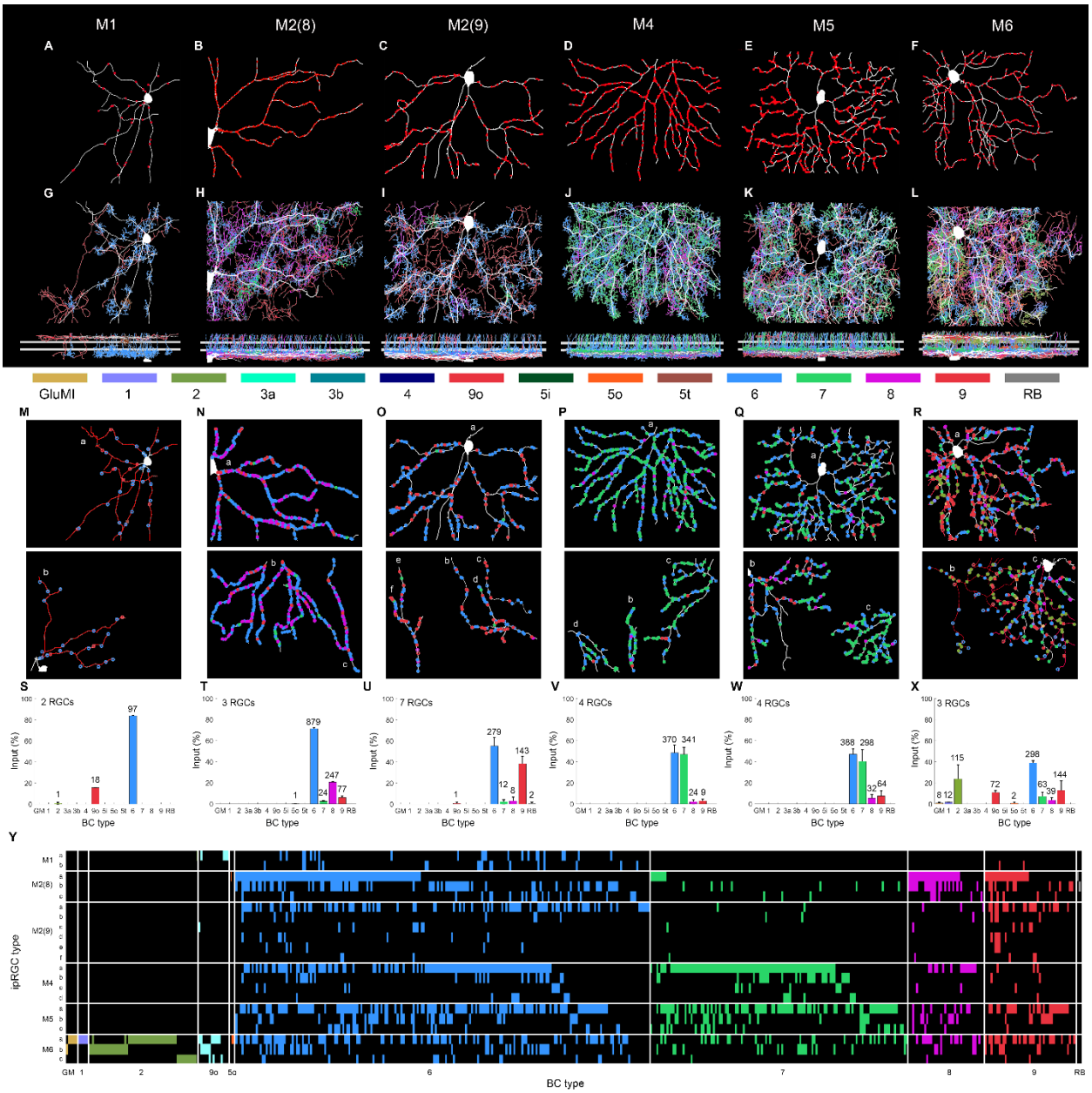

Figure 2. Cone BC Types 6, 7, 8 and 9 provide the bulk input to ipRGCs through either ectopic monad synapses or terminal dyad synapses

A-F. Ultrastructural reconstruction of representative of ipRGCs (*en face* view) and localization of synapses along their dendrites (red dots). **G-L.** Ultrastructural reconstructions of BCs forming synapses onto representative ipRGCs, *en face* view (top) and side view (bottom). RGCs are depicted in white, and each BC type in a unique color (see legend at the bottom). Two horizontal gray stripes mark the ON and OFF cholinergic bands. **M-R**. Summary of BC input onto all identified ipRGCs per type (*en face* view). Ectopic monad synapses and terminal dyad synapses are depicted as empty and solid circles, respectively. Representative ipRGCs from (F-J) appear in the top raw; additional ipRGCs of a given type appear in the bottom row and are numbered. ON input to M6 cells arrived through both ectopic monad synapses along the outer arbor (indicated as empty circles) and terminal dyad synapses along the inner arbor (solid circles) (**R**).

S-X. Percent BC input to ipRGCs; values appearing above bars represent the total number of synapses per BC types. **Y.** BC-ipRGC connectivity matrix, showing the BCs synapsing on 21 ipRGCs.

The patterns of input to ipRGCs from specific BC types could be predicted from their respective stratification profiles and the terminal field area of BCs (Figure 3A). Overall, BCs provided input to ipRGCs that co-stratified with them, with no obvious selectivity (Figure 3B,C). The exception was the M1 type, which received almost no OFF BC input despite stratifying in the far outer IPL where OFF BC terminals dominate (Figure 3B,C). In conclusion, ipRGCs derive their excitatory synaptic input almost entirely from ON cone BCs of Types 6, 7, 8 and 9 through ectopic *en passant* monads or terminal dyads. They lack input from four BC types stratifying in the mid-IPL (Types 5i, 5o, 5t and XBC) and except for M6 cells also lack input from all OFF BC types. This supports the view that BCs supporting that light intensity-encoding signaling in ipRGCs are distinctive.

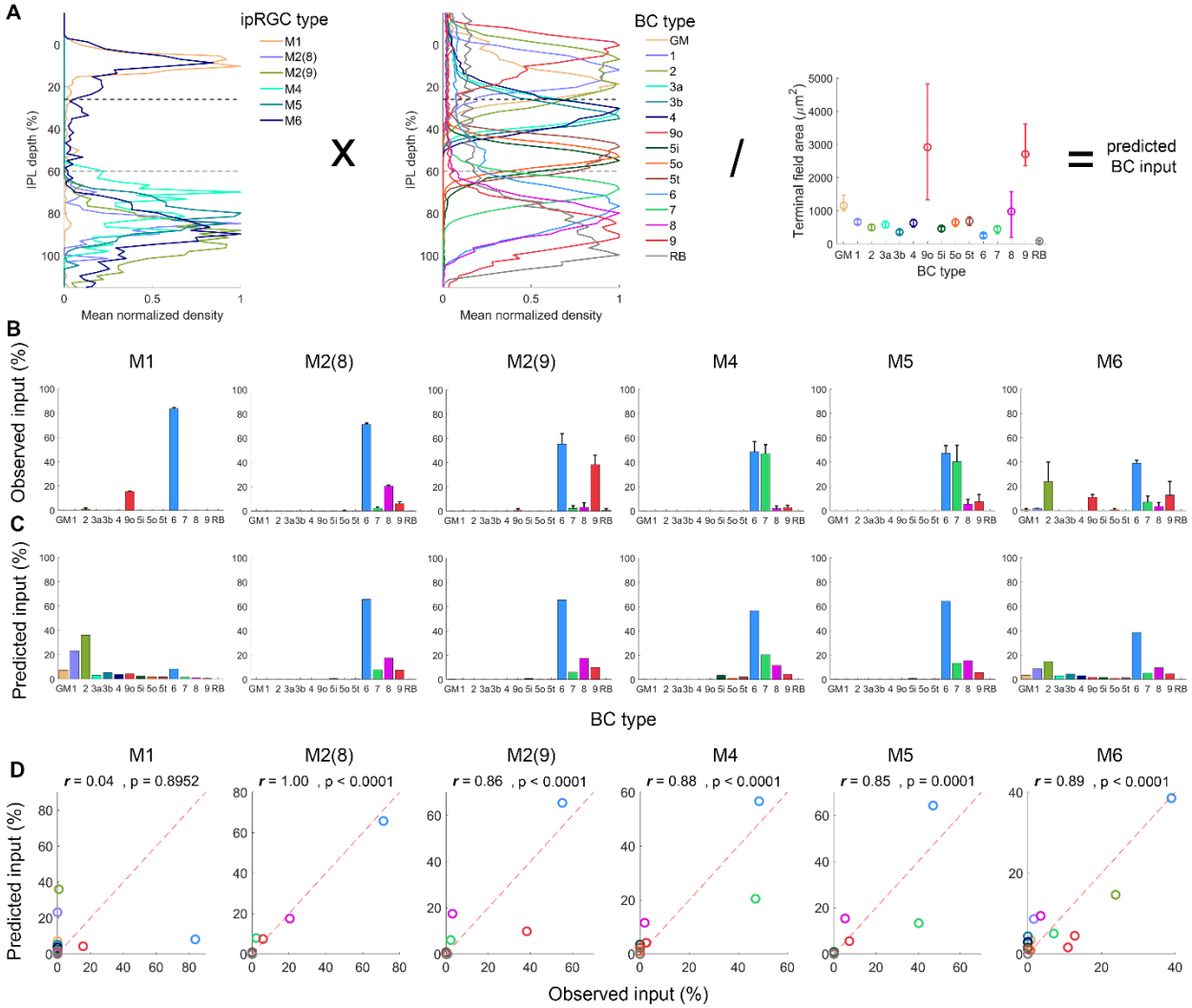

Figure 3. BC-to-ipRGC selectivity based on stratification depth

A. Input patterns from BCs to ipRGCs could be predicted by their stratification depth and BCs' terminal field area. **B,C.** Observed (B) and predicted (C) BC input to M1-M6 ipRGCs. **D.** Predicted vs. observed BC input to ipRGCs. Red dashed diagonals (exact match between predicted and observed % input) mark the identity line. Pearson correlation coefficients and associated p-values are indicated for each ipRGC type.

Glutamate release encodes light intensity in all IPL sublayers, not only those serving ipRGCs

To test the hypothesis that bipolar types driving ipRGCs are specialized to encode intensity, we asked whether local glutamate release encodes intensity best in the IPL sublayers where ipRGCs get their bipolar drive. We expressed the genetically-encoded glutamate indicator iGluSnFR

(Marvin et al., 2013) in large numbers of RGCs and amacrine cells, mostly with somas in the ganglion cell layer (GCL). 2-photon microscopy revealed iGluSnFR-positive dendrites densely filling the IPL (Figure S3F). We tracked the iGluSnFR signal during sequential 30-sec epochs at one of five intensities, and at one of 10 focal planes from the inner nuclear layer (INL; depth 0%) to the GCL (depth 100%) (Figure 4). At depths where ipRGCs get their dominant bipolar input (~65-75%), the glutamate signal was clearly intensity-coding; it persisted throughout the 30-sec stimulus and exhibited a sigmoid intensity-response function. Figure 4A plots the steady-state fluorescence (averaged over the last 5 sec) against irradiance, fit by a Naka-Rushton function (Naka and Rushton, 1966). Surprisingly, the glutamate signal was sustained and intensity-coding at nearly all depths, including the ON ChAT band where many transient RGCs arborize, and throughout the outer (OFF) IPL sublayer as well, where increasing intensity monotonically *decreased* the iGluSnFR signal (Figure 4A). Sustained increases in iGluSnFR signal could be evoked in the OFF sublayer by presenting dark spots on a bright background (Figure S5). Intensity coding was lacking only near the boundary between the ON and OFF sublayers (depth 45%). At that depth, glutamate release exhibited both ON and OFF transients (Figure 4A, middle left). This evidently reflects the summed contributions of ON and OFF BCs. Thus, even at this depth we cannot rule out steady-state ON and OFF intensity signals, which could cancel each other out (Figure 4B-D). In the outer OFF sublayer (depths 5%-25%), we observed a transient release at light onset, presumably reflecting glutamate release from ON-BCs, especially Types 6 and 9o, at ectopic ribbon synapses.

To compare intensity-encoding capacity as a function of IPL depth, we defined two indexes: one for persistence (the ratio of final to initial fluorescence signal during the light step); and the other for magnitude (the difference in steady-state glutamate release in response to the lowest and highest light intensities; Methods). Both indexes exhibited two maxima in their depth profiles (Figure 4E,F), with peaks centered on the middle of the ON and OFF sublayers and separated by a minimum near the ON/OFF sublaminar border. The ON peak overlapped substantially the depths where ipRGC dendrites get Type 6,7, 8 and 9 BC input (65-75%), but also encompassed the ON ChAT band, where direction-selective ganglion cells, which lack intensity coding, stratify. In the outer (OFF) IPL, glutamate release was almost perfectly sustained throughout, and not only in accessory ON sublayer where ipRGCs get ectopic ON-BC input (Figure 4F). Figure

4G-I plots depth profiles for the sensitivity and dynamic range of the steady-state response and the goodness of the Naka-Rushton fit from which they were inferred.

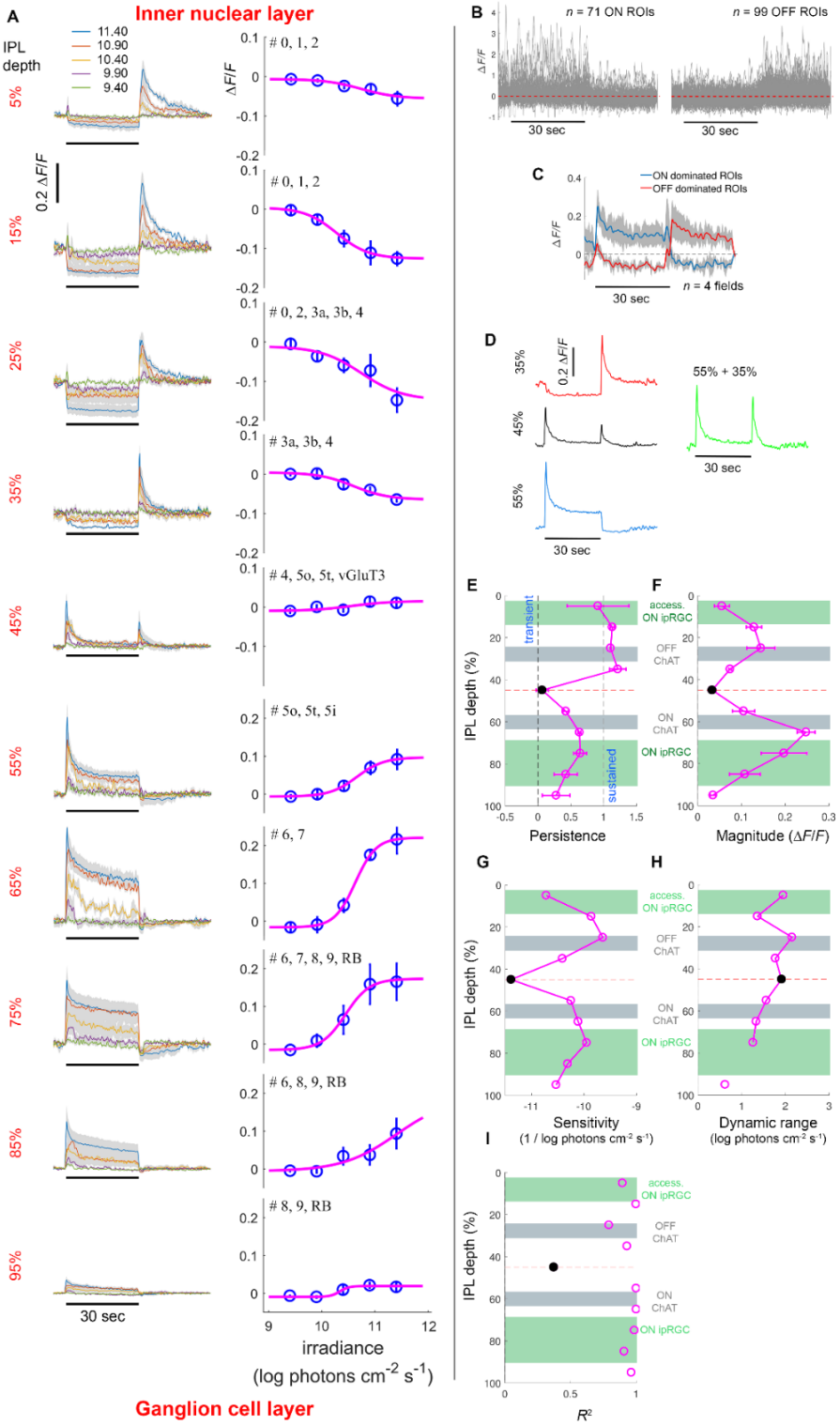

Figure 4. Glutamate release across the IPL is sustained and intensity-encoding

A. Glutamate release at 10 different IPL depths, presumably from BCs and ACs, measured with the fluorescence indicator iGluSnFR in response to 30-sec light steps (horizontal bar) at 5 intensities, depicted in different colors (log photons cm^{-2} s^{-1}), and averaged across the entire field of view (84x42 μm). Left column: glutamate response ($\Delta F/F$) as a function of time. Right column: steady-state glutamate response ($\Delta F/F$; mean response over the last 5 seconds of the stimulus) as a function stimulus intensity. Names of BC types whose mean normalized stratification density at a given IPL depth, as estimated from SBEM reconstruction, exceeded 20% are indicated. In the inner IPL (55%-95% depth), glutamate response typically started with a large-amplitude transient, and then gradually rolled off until the end of the stimulus, upon which glutamate release abruptly dropped. At certain inner IPL depths, the glutamate release became more sustained as stimulus intensity increased. In the outer IPL (5%-35% depth), glutamate release dropped abruptly at the onset of the stimulus, and stayed virtually constant until the termination of the stimulus, upon which glutamate release abruptly increased above baseline and spiked. **B**, **C**. Glutamate release in selected single dendrites, peaking either at light onset or offset, but never at both. **D**. The computationally summed glutamate release of IPL depths 35% and 55% (green), compared to release recorded from the depth of 45% where inner-outer transition occurs (black). **E**. Glutamate release is almost perfectly sustained in the outer IPL; in the inner IPL, it is the most sustained at depths 65% and 75% and becomes more transient toward the ON-OFF IPL boundary and the IPL-GCL boundary. **F**. Steady state glutamate release magnitude (maximum - minimum release recorded across the stimulus intensities) was minimal at the ON-OFF IPL boundary, largest at the middle of the outer and inner IPL (depths 25% and 65%, respectively), and decreased toward both IPL edges. The depths of highest magnitude coincide with the ON and OFF ChAT bands. **G**. Sensitivity of glutamate release (see Methods) was minimal at the ON-OFF IPL boundary, largest at the middle of the outer and inner IPL, and decreased toward both IPL edges. **H**. The dynamic range of steady state glutamate responses (see Methods) varied slightly across the IPL. **I**. Naka-Rushton function goodness of fit was high across the IPL except for the ON-OFF transition depth.

To assess the role of amacrine-cell inhibition in shaping intensity coding in BC output, we repeated the experiments of Figure 4 while blocking GABA and glycine receptors with picrotoxin and strychnine. Inhibitory blockade minimally affected the persistence and intensity-encoding capacity of BC glutamate release (Figure S6). This implies that light intensity signals in BCs are shaped not mainly by inhibition but rather by other factors, such as glutamatergic signaling kinetics at the photoreceptor synapse and intrinsic membrane properties or synaptic release mechanisms at BC axon terminals.

Taken together, our results show that the excitatory input to ipRGCs derives from specific BC types. Though these types encode light intensity, such intensity signals are present across the IPL sublaminae and BC types, both ON and OFF, and not a unique feature of the types innervating

ipRGCs. This suggests that the differing capacities of ipRGCs and other RGCs for intensity coding lie postsynaptically, in the way RGCs respond to bipolar excitation.

Multiple postsynaptic mechanisms suppress intensity signals in the spiking output of conventional ON RGCs

To probe postsynaptic mechanisms contributing to the unique intensity-coding feature of ipRGCs, we compared the glutamate released onto specific RGC types with the postsynaptic excitatory currents and firing rate this evoked (Figure 5). We compared the M4 ipRGC (ON alpha) with a conventional RGC type, the ON direction-selective cell (ON-DSGC). The two are both ON-type and stratify at very nearly the same depth (Figure 5A,B), but while the ON-DSGC is among the most sustained of conventional ON RGCs (Baden et al., 2016), it does not encode intensity in its spike train as the M4 cell does. We used Cre driver mice (Ecker et al., 2010; Lilley et al., 2019) and intravitreal injections of a Cre-dependent viral vector to express iGluSnFR selectively in one or the other of these RGC types (Methods). We made patch recordings of excitatory currents and spiking in these RGCs *in vitro*. A contrasting dye was included in the pipette, revealing their dendrites so that iGluSnFR imaging could be directed to them specifically (Figure 5F,I) and for subsequent reconstruction of cell morphology (Figure 5C). Direction selectivity was confirmed for the ON-DSGC with drifting grating stimuli (Figure 5Q).

Light spots on dark backgrounds evoked sustained, intensity-dependent glutamate input to both cell types, as inferred from their iGluSnFR signals (Figure 5F,I,L). However, over the course of the 30-sec stimulus, ON-DSGCs exhibited more attenuation of their iGluSnFR signal than did M4 cells and response saturation for intense stimuli which the M4 cell lacked (Figure 5L), presumably reflecting distinct glutamate release kinetics among presynaptic BCs. These differences were accentuated in the recordings of postsynaptic excitatory currents. In M4 cells the currents lasted throughout the stimulus and tracked light intensity, while those of ON-DSGCs were transient, approaching baseline after only 5-10 s (Figure 5G,J,M), and lacked obvious intensity-coding. Firing rates mirrored this difference in the excitatory drive (Figure 5H,K,N).

Intensity coding as assayed by the persistence index was well maintained in M4 ipRGCs across these stages of signaling (Figure 5O, red). The intensity signal was filtered out in at least two stages in ON-DSGCs (Figure 5O, blue). There was a particularly marked difference between sensed glutamate (iGluSnFR) and resulting excitatory drive (patch-recorded current). There was also a more modest one between current and spiking. Significant filtering occurs between glutamate, currents, and spiking, because the excitatory currents in ON-DSGCs differed significantly in persistence index from that for firing rate as well as that for the local glutamate concentration (see figure caption for detailed statistics).

We also used the magnitude index described above to compare the abilities of ON-DSGCs and M4 cells to encode intensity at various stages. Beginning at the level of the iGluSnFR glutamate-input signal, the ON-DSGC magnitude index was already only half that in M4 ipRGCs. At subsequent stages the fraction declined progressively, first for the resulting excitatory current and once more for spiking (Figure 5P). These declines were statistically significant (see figure caption for detailed statistics).

We conclude that a highly non-linear relationship between steady-state glutamate concentration and excitatory current in ON-DSGCs plays the main role in filtering out intensity signals in the ON-DSGC spike train, though this is supplemented by more transient bipolar drive and at least one additional downstream non-linearity. The M4 ipRGC lacks these pronounced non-linearities and thus reports the bipolar intensity signal.

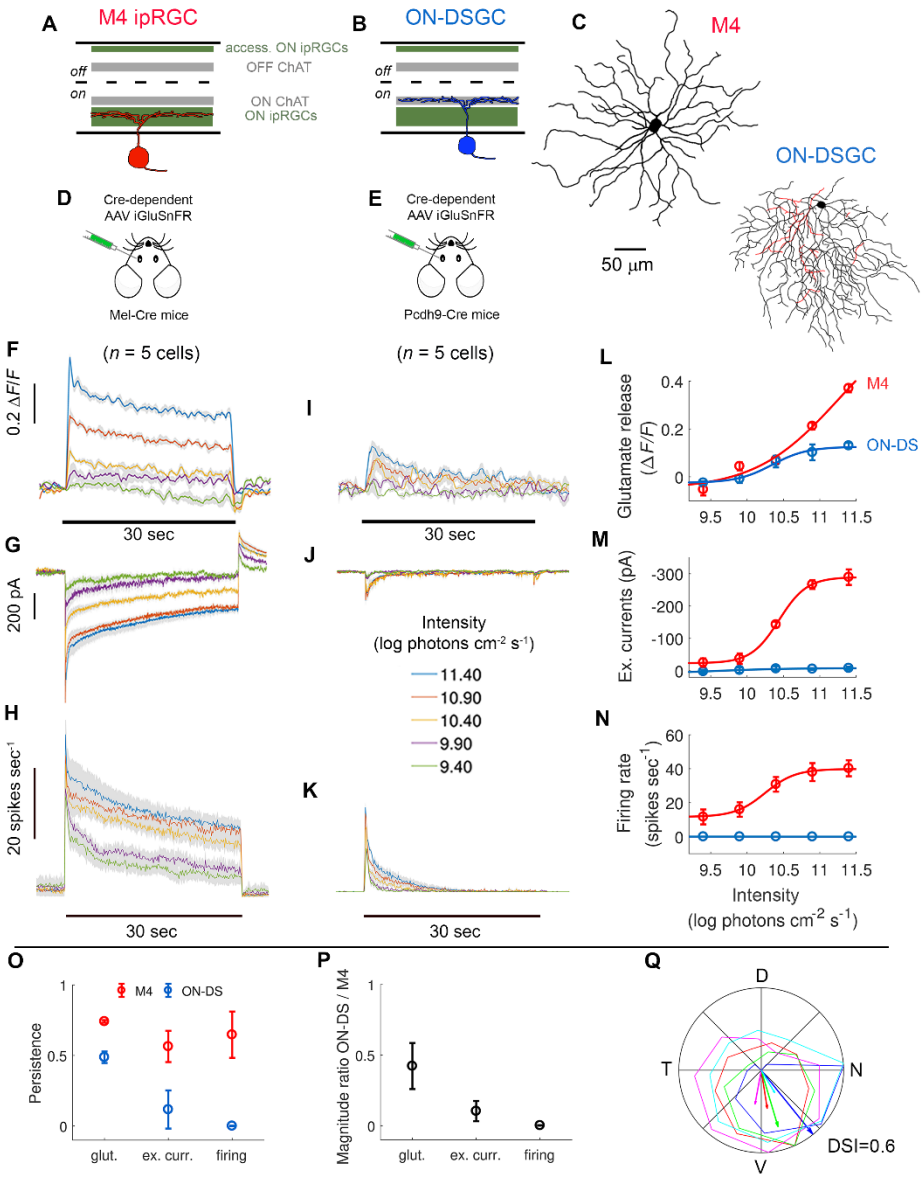

Figure 5. Capacity for intensity encoding decreases postsynaptically in ON-DSGCs more than in M4 ipRGCs

A, **B**. M4 ipRGC stratifying at the ON plexus of ipRGCs (**A**) and ON-DSGC, stratifying at the ON cholinergic band and somewhat at the OFF cholinergic band (**B**). **C.** Reconstructions of genetically- and functionally-identified M4 and ON-DSGC. **D**, **E**. Intravitreal injections of Cre-dependent iGluSnFR AAVs in either Mel-Cre (for M4) or Pcdh9$^{Cre/+}$ (for ON-DSGCs) mice allowed targeting. **F-H, I-K**. Glutamate release, excitatory currents, and firing rate as a function of stimulus intensity in response to 30-sec bright spots over dark background, for M4 (F-H) and ON-DSGCs (I-K). **I-N**. Intensity-response curves for the glutamate release onto (**F**), and excitatory currents (**G**) and firing rate (**H**) of M4 ipRGCs (red) and ON-DSGCs (blue). **O**. Response persistence of M4 ipRGCs and ON-DSGCs. In contrast to ON-DSGCs for which response persistence differed acorss transmission stages (permutation one-way ANOVA, $p < 0.001$; glutamate, 0.48 ± 0.04; excitatory currents, 0.12 ± 0.13, firing rate, 0.00005 ± 0.001; mean ± s.d.; post-hoc analysis: excitatory currents vs. firing rate, $p = 0.007$; excitatory currents

vs. glutamate release, p = 0.006), response persistence for M4 ipRGCs did not differ significantly and decreased only slightly when moving between the signal transmission stages (permutation one-way ANOVA, p = 0.38; glutamate, 0.74 ± 0.009; excitatory currents, 0.56 ± 0.11, firing rate, 0.65 ± 0.16; mean ± s.d.). **P.** Ratio of the steady-state magnitude between M4 ipRGCs and ON-DSGCs was higher for glutamate release, lower for excitatory currents, and lowest for firing rate (permutation one-way ANOVA, p < 0.001; glutamate, 0.42 ± 0.163; excitatory currents, 0.10 ± 0.071, firing rate, 0.002 ± 0.002; mean ± s.d.; post hoc analysis: each of the possible treatment pairs differed significantly, p < 0.001). **Q.** Polar plot shows response amplitude (normalized to maximum) for each direction; each cell depicted in a different color. The direction and length of vectors indicate the preferred direction and direction selectivity index (DSI) of cells, respectively (N, nasal; D, dorsal; T, temporal; V, ventral).

Filtering of intensity signals in conventional OFF RGCs

We used the same approach to assess intensity-encoding at the same stages in two additional conventional RGCs that receive OFF-BC excitatory input: ON-OFF-DSGCs and OFF αRGCs. In the same SBEM volume, we reconstructed an ON-OFF-DSGC and mapped its bipolar inputs, as we had for ipRGCs (Figure S7). This cell received input predominantly from ON-BC Types 5o, 5t, and 5i and from OFF-BC Types GluMI, 2, 3a, 3b, and 4 (Figure 6V-X, AB). For these functional experiments, we expressed iGluSnFR widely among RGCs as earlier, then targeted RGCs of appropriate size for patch recordings. ON-OFF-DSGCs were recognizable from their direction-selective responses to grating motion and characteristic bistratified morphology as revealed by dye filling and 2-photon imaging (Figure 6F). Dye filling allowed us to limit our regions of interest to the iGluSnFR signal arising from dendrites of the patched cell. We first recorded the iGluSnFR response from ON arbor dendrites. The glutamate signal evoked by light spots on a dark background was sustained and intensity-dependent but the postsynaptic excitatory current was not (Figure 6A-C), replicating the pattern observed earlier for ON-DSGCs (Figure 5). Turning to the OFF arbor of the same cell, we found the same light spots evoked sustained, intensity-encoding reductions in iGluSnFR signals (Figure 6D), while dark spots on a bright background induced sustained intensity-dependent increases (Figure 6G-I). In contrast, the excitatory currents evoked by these same stimuli were transient, peaking at both stimulus onset and offset, reflecting the summed ON and OFF bipolar inputs to the bistratified arbor (Figure 6B,H). Thus, in ON-OFF-DSGCs, OFF bipolar inputs carrying substantial intensity signals are strongly filtered out at the level of excitatory currents, and the same occurs for ON bipolar input, as seen earlier for ON-DSGCs.

We probed a pure OFF RGC in the same way, targeting OFF αRGCs for study. This type stratifies between the ON and OFF ChAT bands (35% depth), close to the ON/OFF sublaminar boundary. Our SBEM analysis of one OFF αRGC revealed input from OFF-BC Types 3A, 3B and 4 (Figure 6Y,Z,AA,AB). In functional studies, bright spots over a dark background triggered a sustained, intensity-coding reduction in the glutamate released onto the cell, mirroring the results averaged across all dendrites at the same IPL depth (compare Figure 6J,L and Figure 4 at 35% depth). The same dendrites exhibited an increased glutamate release at the onset of a dark spot which lasted as long as the stimulus, but did not correlate with stimulus intensity (Figure 6M,O). The excitatory currents showed weaker versions of the same trends for both light and dark stimuli (Figure 6K,N,L,O). Therefore, the intensity-encoding signal from BCs to these OFF αRGCs is *preserved* at the level of excitatory currents. The connectivity selectivity from BCs to the OFF αRGC and ON-OFF-DSGC could not be accurately predicted in our modeling (Figure S7J-M). In conclusion, our results for the three conventional RGC types examined (ON-DSGC, ON-OFF-DSGC, and OFF αRGCs) indicate that the key locus for temporal filtering of sustained intensity-encoding signals is postsynaptic to the BC axon terminal, and, depending on cell type, occurs at the synapse or downstream, via filtering strategies which differ between conventional RGC types.

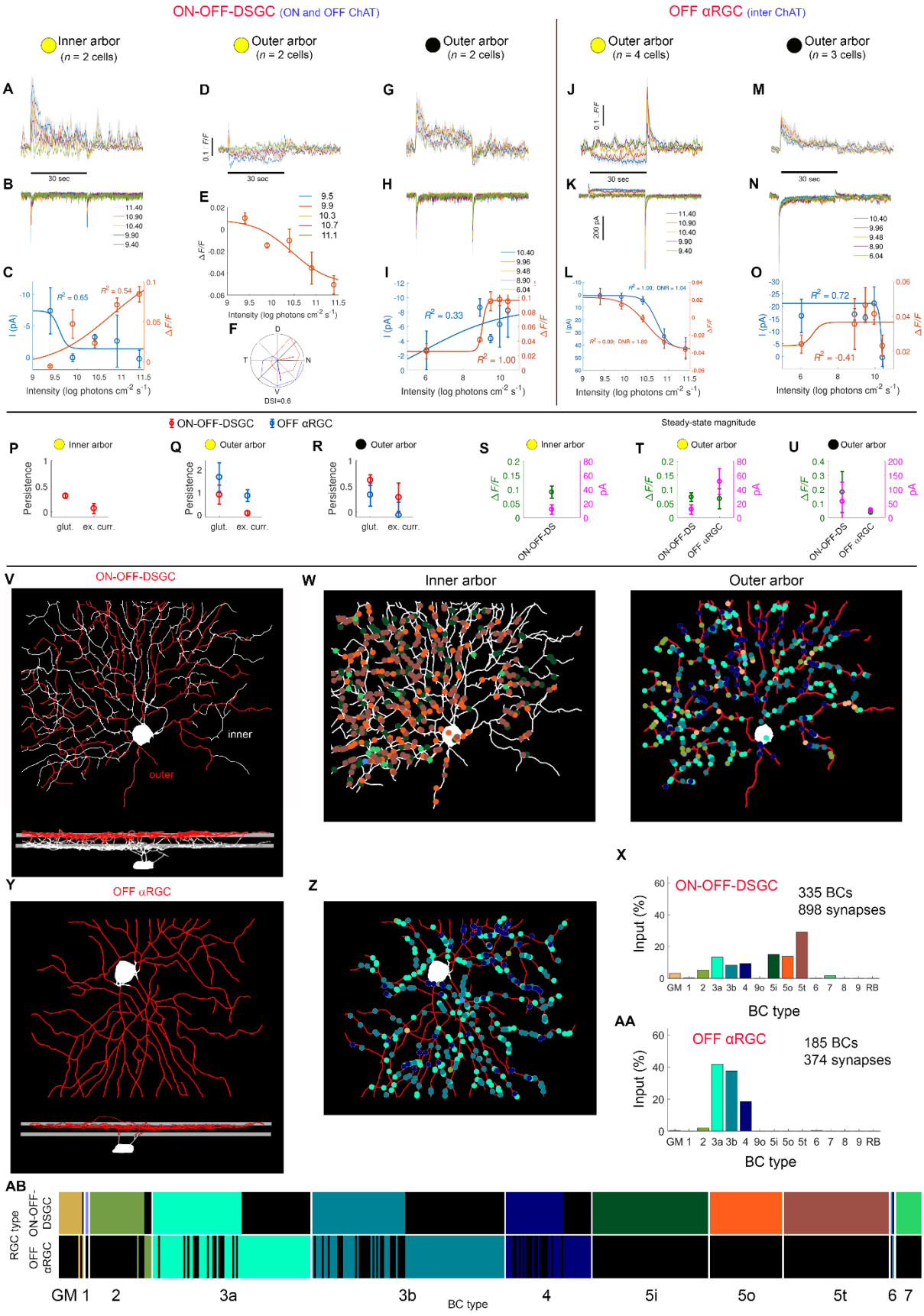

Figure 6. Sustained and intensity-encoding glutamate release onto conventional RGCs

Following intravitreal injection of constitutive iGluSnFR AAVs to wildtype mice, iGluSnFR-positive cells were patched with red dye for arbor identification. Intensity encoding of ON-OFF-DSGCs was assessed by glutamate release ($\Delta F/F$) onto inner-IPL dendrites (A) or outer-IPL dendrites (D, G) and concurrently recording excitatory currents, in response to 30 sec of light (horizontal bar) at 5 intensities (depicted in different colors; log photons cm^{-2} s^{-1}), administered as bright spots on a dark background (A-E) or dark spots on a bright background (G-I). Excitatory currents were recorded while holding the membrane voltage at the chloride reversal potential. **A, B.** Excitatory currents and simultaneous glutamate release onto inner-IPL dendrites of ON-OFF-DSGCs in response to bright spots over a dark background. **C**. Steady-state response (mean over last 5 sec of stimulus) as a function of stimulus intensity for glutamate release ($\Delta F/F$, orange) and excitatory currents (pA, blue, y-axis inverted to facilitate comparison to glutamate response). Goodness of fit to the Naka-Rushton function is indicated. **D, E**. Glutamate release onto outer-IPL dendrites of ON-OFF-DSGCs. **F**. Direction selectivity of ON-OFF-DSGCs. Polar plot shows response amplitude (normalized to maximum) for each direction; each cell depicted in a different color. The direction and length of vectors indicate the preferred direction and direction selectivity index (DSI) of cells, respectively (N, nasal; D, dorsal; T, temporal; V, ventral). **G**-**I**. Simultaneous excitatory currents and glutamate release onto outer-IPL dendrites of ON-OFF-DSGCs in response to dark spots of 5 intensities (depicted by different colors) over a bright background (12.5 log photons cm^{-2} s^{-1}). **J**-**O**. Intensity encoding of OFF αRGCs in response to bright spots on a dark background (J-L) or dark spots on a bright background (M-O). **P**-**R**. Persistence of glutamate release (glut.) and excitatory currents (ex. curr.) in response to bright spots over a dark background and dark spots over a bright background. Glutamate release readings are indicated for dendrites in the ON arbor (P) and OFF arbor (Q,R). **S**-**U**. Magnitude of steady-state glutamate release (left y-axis, green) and excitatory currents (right y-axis, magenta) in response to bright spots over a dark background and dark spots over a bright background. Glutamate release readings are indicated for dendrites in the ON arbor (S) and OFF arbor (T,U). **V**. SBEM reconstruction of an ON-OFF-DSGC as viewed at the plane of the retina (top) and orthogonally (bottom). Horizontal stripes mark the ON and OFF cholinergic bands. **W.** Reconstruction of BC input onto the ON-OFF-DSGC. The inner and outer arbors of the RGC are depicted in white and red, respectively; each BC type is depicted in a unique color. Red circles denote ribbon synapses (empty circles, monad synapses; filled circles, dyad synapses). **X**, Percent input of each BC type to the presumptive ON-OFF-DSGC. **Y**,**AA,AB**. SBEM reconstruction of BC input onto an OFF αRGC.

Ectopic synapses transmit sustained and intensity-encoding signals

In the course of conducting the SBEM reconstruction and physiological characterization, we revealed the ubiquitous nature of ectopic monad synapses. M1 ipRGCs stratify only in the far outer IPL (5-15% depth) and thus receive their ON-BC input only through ectopic monad synapses (Figure 2A,E). We showed that excitatory currents in these M1 cells, that integrate rod/cone synaptic input with intrinsic melanopsin sensitivity, are sustained and intensity

encoding (Figure S1). However, the kinetics of glutamate release at ectopic synapses has never been examined directly. To measure the glutamate release at ectopic synapses, we utilized intravitreal injections of Cre-dependent iGluSnFR AAVs in the Opn4$^{Cre/+}$ mouse (Figure 7A). This approach labels only a limited number of dendrites at the far outer IPL, where M1, M3, and M6 ipRGCs stratify. We recorded the iGluSnFR glutamate signal from selected dendrites, and later reconstructed and classified the parent cells from a 2-photon depth series. The glutamate released onto labeled ipRGC dendrites in the accessory ON sublayer was sustained and intensity-encoding (Figure 7B). Many of these cells exhibited dendritic arbors too dense to be M1s or M3s and presumably were M6 ipRGCs, which we have shown receive ectopic ON-BC synapses (Figure 2). Therefore, the observed light-evoked glutamate release at the far outer IPL (where the axon terminals of OFF-BCs stratify) demonstrates that ectopic synapses transmit ON-polarity, sustained, intensity-encoding light signals.

Finally, to compare the kinetics of glutamate release between ectopic monad synapses and terminal dyad synapses, we compared glutamate release at ectopic synapses to the glutamate release onto M4 and M5 ipRGCs that receive their BC input predominantly from dyad contacts in the inner IPL (65%-75% depth). Glutamate released onto M5 cells was measured using the same approach applied for M4 cells (Figure 5). The persistence of glutamate release differed significantly between ectopic monad synapses and terminal dyad synapses formed with M4 and M5 ipRGCs, being lowest at ectopic synapses (Figure 7D-F; permutation one-way ANOVA [PA], $p < 0.001$; M4, 0.74 ± 0.009; M5, 0.63 ± 0.043; ectopic synapses, 0.33 ± 0.241; mean ± s.d.). Post-hoc analysis revealed that each of the possible treatment pairs differed significantly (M4 vs. M5, PA, $p = 0.036$; M4 vs. ectopic synapses, $p = 0.022$, M5 vs. ectopic synapses, $p = 0.025$). Likewise, the steady-state magnitude of glutamate release in response to the highest light intensity also differed significantly, again, being lowest at ectopic synapses (PA, $p = 0.001$; M4, 0.24±0.101; M5, 0.19±0.054; ectopic synapses, 0.09±0.053; mean ± s.d.), including for each possible treatment pair (post-hoc analysis of M4 vs. M5, PA, $p = 0.016$; M4 vs. ectopic synapses, $p = 0.003$, M5 vs. ectopic synapses, $p = 0.005$). This demonstrates that ectopic monad synapses are capable of transmitting sustained, intensity-encoding signals, but at a reduced capacity compared to terminal dyad synapses.

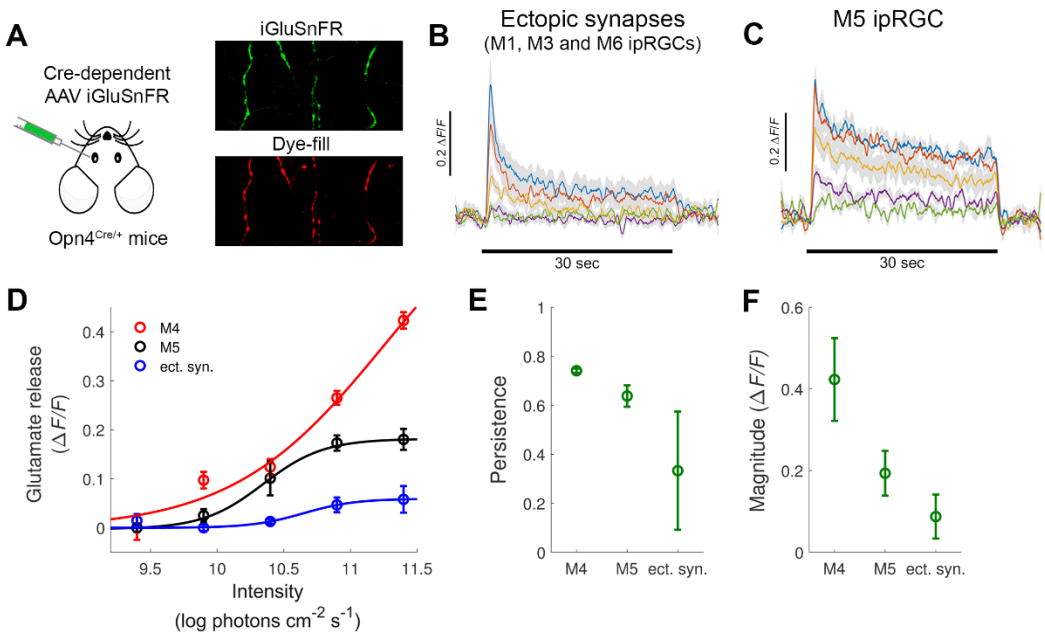

Figure 7. Sustained intensity-encoding glutamate release at ectopic synapses

A. Glutamate release was measured at ectopic synapses onto ipRGCs, and at terminal synapses onto M4 and M5 ipRGCs in intravitreally, Cre-dependent iGluSnFR AAVs injected Opn4$^{Cre/+}$ mice, selectively labeling melanopsin-expressing ipRGCs. Imaged are iGluSnFR-positive dendrites (green) in the inner IPL. iGluSnFR-positive cells were patched with red dye; the dyed arbor facilitated M4 and M5 cells identification. **B**, **C**. Glutamate release ($\Delta F/F$) at ectopic synapses (n=9) and onto M5 ipRGCs (n=5) in response to 30 sec of light (horizontal bar) at 5 intensities depicted in different colors (log photons cm^{-2} s^{-1}). **D.** Steady-state glutamate release (mean response over the last 5 sec of the light stimulus), for M4 (n=5, raw data in Figure 4), M5 (n=5), and ectopic synapses (n=9; abbrev. ect. syn.). Glutamate release (mean ± s.e.m), fitted to the Naka-Rushton function. **E.** Persistence (mean ± s.d.) of glutamate release in M4, M5, and ectopic synapses. **F.** Steady-state magnitude of glutamate release (mean ± s.d.) in response to the highest light intensity.

Discussion

Among retinal output neurons, only ipRGCs stably encode environmental light intensity. Here we have delineated the cell types, synaptic circuits, and physiological properties that shape intensity coding in the inner retina and account for the idiosyncratic intensity-dependent spiking of ipRGCs. We demonstrated by SBEM and glutamate imaging that ON bipolar axons make numerous contacts onto ipRGC dendrites in the accessory ON sublayer, and that these contacts transmit intensity signals. In the ON sublayer, we found that ipRGCs get their excitatory synaptic input almost exclusively from a subset of ON bipolar cells (Types 6-9), mostly at dyad contacts.

Only the M6 type gets any noteworthy OFF bipolar input (Type 2), a surprise since only ON responses have been detected electrophysiologically (Quattrochi et al., 2019). Imaging confirmed sustained, intensity-encoding glutamate release onto ipRGC dendrites. To our surprise, though, strong intensity signals were detected by glutamate imaging at nearly all IPL depths and specifically when the glutamate reporter was expressed on conventional RGCs with relatively transient responses and negligible intensity coding. Instead, postsynaptic mechanisms such as nonlinearities in the translation of extracellular glutamate concentration to current, or from current to spiking, are primarily responsible for differentiating the intensity-encoding behavior of conventional RGCs from ipRGCs. In this sense, it is the weakness or absence of such filtering mechanisms in ipRGCs that preserves the bipolar intensity signal, specializing them for physiological and behavioral responses driven by light intensity-dependent signals.

Bipolar cells exhibit sustained intensity-encoding output

Sustained intensity-encoding signals were observed at most depths in the IPL, not only in the inner half of the ON sublayer where most ipRGC types stratify but also throughout most of the rest of the ON IPL and in the OFF IPL. Only subtle differences in the intensity signal were apparent when comparing the terminal strata of most bipolar types. Intensity coding cannot be ruled out even in the mid-IPL near the ON/OFF sublaminar border, because signals there blend ON and OFF contributions, so the opposite signs of the steady-state signal could cancel one another out. Several BC types stratify at each level of the IPL and VGluT3 amacrine cells also presumably contribute to the measured iGluSnFR signal in the mid-IPL (Kim et al., 2015) (35-55% depth). Thus, our data do not provide definitive evidence that all BC types are capable of sustained, intensity-encoding output. Nonetheless, specific postsynaptic RGC types, both conventional and ipRGCs, exhibited sustained intensity coding bipolar drive despite being fed by different complements of bipolar types.

Borghuis et al.(2013) and Baden et al.(2013) recorded the glutamate released from BCs and the calcium responses in BCs, over 0.5 sec (150 μm bright spot) and 4 sec (stimulus diameter not specified), respectively. In agreement with those studies, we find the lowest persistence of glutamate release (i.e, the most transient signal) near the middle of the IPL, at the ON-OFF transition zone. Also in agreement with the prior studies, the persistence of the response evoked

upon termination of the light stimulus (OFF phase) in the outer IPL, was greatest at the far outer IPL (near the INL), and decreased when approaching the ON-OFF transition zone (Figure 4A). However, while previous work reported that the calcium response of BCs and the glutamate released from BCs are most persistent at the IPL-GCL boundary, the current study revealed greater glutamate release persistence in the middle of the inner IPL, close to where ipRGCs stratify (65-75% IPL depth). This discrepancy may have arisen from the differences in stimulus durations, as no previous study examined the glutamate released from BCs (or calcium transients in BCs) under a 30-sec long light stimulus as applied here.

GABAergic and glycinergic feedback played little if any role in the persistence of BC glutamate release, consistent with a previous report (Zhao et al., 2017). Instead, the temporal filtering that differentiates ipRGCs from conventional RGCs is mainly postsynaptic to the BC axon terminal, and likely involves differing glutamate-receptor kinetics in the face of steady glutamate release, and intrinsic membrane properties that determine the spiking response to maintained excitatory currents. The subtle variations in intensity coding among BC output signals could have multiple sources, including cell-type dependence of metabotropic glutamatergic signaling mechanisms, axon terminal biophysics and vesicular glutamate release (Awatramani and Slaughter, 2000; Higgs and Lukasiewicz, 1999; Zhao et al., 2017). Picrotoxin and strychnine did exert subtle effects on glutamate release from BCs, and these may have resulted from alterations in feedback inhibition from ACs onto BCs, or even by modulation of outer retinal signaling (Blanco et al., 1996; Greferath et al., 1995; Greferath et al., 1994; Hughes et al., 1991; Vardi et al., 1992; Wassle et al., 1998).

BC intensity signaling to ipRGCs and conventional RGCs

We found that ipRGCs, except for the M6 cell, receive their synaptic input only from ON-BCs, of predominantly type 6, 7, 8 and 9, through ectopic monad synapses (in the outer IPL) and terminal dyad synapses (in the inner IPL), and that they generally receive synaptic input from BCs that costratify with them, with no obvious specificity. However, the outer-IPL-stratifying M1 ipRGCs received their synaptic input almost exclusively through ectopic synapses and largely avoided axon terminals from OFF-BCs. Such selectivity would be crucial for the ability of M1 cells to convey ON-polarity light information, which is the main drive for the pupillary

light reflex, circadian photoentrainment, and light-dependent mood regulation (An et al., 2020; Chen et al., 2011; Fernandez et al., 2018).

The glutamate released onto dendrites of ipRGCs was sustained and intensity-encoding. In support of our finding obtained using wide-field glutamate imaging across the IPL, the glutamate signal was also sustained and intensity-encoding for three types of conventional RGCs (ON-DSGC, ON-OFF-DSGC, and OFF αRGC) which stratify both within the ON and OFF ChAT bands and between them, and exhibiting diverse patterns of BC input. While BC-to-RGC connectivity could be roughly modeled based only on the stratification profiles of RGCs and BCs together with the BCs terminal field area, the input patterns from BCs to ipRGCs and to conventional RGCs could not be fully explained by such a model, indicating that BC-to-RGC connectivity is dependent to some extent on cell-type identity and not merely stratification.

Conventional RGCs are optimized for the transmission of spatiotemporal contrast in support of the detection and recognition of objects, color and motion (Baden et al., 2016), while ipRGCs encode intensity. Still, these two seemingly distinct components of the retinal light encoding of visual information also appear to interact during light adaptation, which allows the retina to encode contrast over a broad range of light intensities. ipRGCs are known to inject intensity signals back into retina by chemical synapses onto dopaminergic ACs (Zhang et al., 2008) which, in turn, modify the functional properties of retinal neurons through dopaminergic signaling, modulating the dynamic range over which the retina operates (Dowling, 1987). Additionally, ipRGCs have been recently shown to inject their intensity signals through gap junctions to a family of spiking polyaxonal ACs whose somata are unconventionally placed in the ganglion cell layer (Reifler et al., 2015; Sabbah et al., 2017a). However, whether these intensity signals are further transmitted within the retina and modulate its sensitivity has not been clarified to date. A broader conceptual framework for retinal signal processing can thus be offered based on these results, in which retinal-wide filtering is hypothesized to continuously subtract from light signals a magnitude inversely proportional to the light intensity, a filtering process permitting conventional RGCs to remain within their operational range in a constantly changing environment.

See *Supplementary Discussion* on ipRGC excitatory synaptic currents, cell type identification, and intensity encoding at ectopic monad synapses vs. terminal dyad synapses.

Acknowledgements

We thank Alex Kolodkin for kindly providing us with the Pcdh9$^{Cre/+}$ mice. We are thankful to our colleagues who provided invaluable theoretical, data-analytic and technical advice, Jim McIlwain, Bart Borghuis, Geoff Williams, Scott Cruikshank, Maureen Estevez Stabio, Shane Crandall, and Eli Shmueli; Dianne Boghossian for genotyped experimental mice; Loren L. Looger, Janelia Research Campus, Howard Hughes Medical Institute for sharing the iGluSnFR glutamate indicator. This project was supported by the Banting Postdoctoral Fellowship of Canada to S.S., The Sidney A. Fox and Dorothea Doctors Fox Postdoctoral Fellowship in Ophthalmology and Visual Sciences to S.S., The United States-Israel Binational Science Foundation grant (#2019209) awarded to S.S., and NIH grant (R01 EY12793) and an Alcon Research Institute Award to D.M.B.

Author Contributions

S.S. and D.M.B. designed the study and developed the theoretical framework. S.S. performed all imaging, electrophysiological recordings, and intracellular dye-fills. S.S., E.K., G.M., M.B. and T.Z. performed intravitreal injections. S.S., D.M.B., C.P., I.B., H.R., J.C., E.K., M.B., C.E., A.N.G., L.C., M.T.K., G.M., A.B.L., T.Z., and H.D. traced and classified retinal neurons from a serial block-face electron microscopy data set and light microscopic depth series, and performed immunostaining of retinas. S.S. analyzed all morphological, electrophysiological, and functional imaging data. S.S. and D.M.B. wrote the paper.

Correspondence and requests for materials should be addressed to shai.sabbah@mail.huji.ac.il or david_berson@brown.edu

Methods

Animals

All procedures were in accordance with National Institutes of Health guidelines and approved by the Institutional Animal Care and Use Committee at Brown University. We used adult (2-2.5 months old; either sex) wildtype C57BL/6J mice (Jackson Laboratory) and the melanopsin reporter strain Opn4$^{Cre/+}$ (Ecker et al., 2010) that marks ipRGCs, donated by Dr. Samer Hattar, the National Institute of Mental Health.

Intravitreal injections of glutamate fluorescent indicator

Mice (C57BL/6J, Opn4$^{Cre/+}$, or Pcdh9$^{Cre/+}$) were anesthetized with isoflurane (3% in oxygen; Matrx VIP 3000, Midmark). Two viral vectors inducing expression of the glutamate indicator iGluSnFR were used (Vector Core, UPenn; 1.5 –2 µl of ~10^{12} units/ml): a Cre-dependent vector (AAV1.CAG.Flex.iGluSnFR) and a non-specific one (AAV1.hSyn.iGluSnFR). Viral vectors were injected into the vitreous humor of the right eye through a glass pipette using a microinjector (Picospritzer III, Science Products GmbH). Animals were euthanatized and retinas harvested 14-21d later.

Tissue harvest and retinal dissection

Eyes were removed and immersed in oxygenated Ames medium (95% O_2, 5% CO_2; Sigma-Aldrich; supplemented with 23 mM $NaHCO_3$ and 10 mM D-glucose). Under dim red light, the globe was cut along the ora serrata, and cornea, lens and vitreous removed. Four radial relieving cuts were made in the eyecup. The retina was flat-mounted on a custom-machined hydrophilic polytetrafluoroethylene membrane (cell culture inserts, Millicell) (Ivanova et al., 2013) using gentle suction, and secured in a chamber continuously superfused with oxygenated Ames' medium (32–34°C) on a microscope stage.

Two-photon functional glutamate imaging

Glutamate imaging and whole-cell recordings were conducted on a multiphoton Olympus FV1200MPE BASIC (BX-61WI) microscope equipped with a 25x, 1.05 NA water-immersion objective (XLPL25XWMP, Olympus) and an ultrafast pulsed laser (Mai Tai DeepSee HP, Spectra-Physics) tuned to 910 nm. Epifluorescence emission was separated into "green" and

"red" channels with a 570 nm dichroic mirror and a 525/50 bandpass filter (FF03-525/50-32, Semrock, green channel) and 575-630 nm bandpass filter (BA575-630, Olympus, red channel), respectively. The microscope system was controlled by FluoView software (FV10-ASW v.4.1). Images of 256x128 pixels representing 84x42 μm on the retina were acquired at 15 Hz (zoom setting of 6).

We pharmacologically blocked receptors and pathways with L-AP4, a group-III metabotropic glutamate receptor agonist acting on the metabotropic glutamate receptor mGluR6; D-AP-5, a NMDA glutamate receptor antagonist; DNQX, an AMPA/kainate glutamate receptor antagonist; ACET, a selective GluR5-containing kainate-receptor antagonist; picrotoxin, a non-competitive channel blocker for $GABA_A$ receptors; or strychnine, a glycine receptors antagonist, all purchased from Tocris.

Visual stimuli

Patterned stimuli, generated with a Matlab Psychtoolbox (MathWorks), were focused onto outer segments of photoreceptors and projected (AX325AA, HP) through the microscope's condenser (Borghuis et al., 2013). The projected stimulus covered 1.5x1.5 mm of retinal surface with 5×5 μm pixels. The video projector was modified to use a single UV LED (NC4U134A, Nichia). The LED's peak wavelength (385 nm) shifted to 395 nm after transmission through a 440 nm short-pass dichroic filter (FF01-440/SP, Semrock), a dichroic mirror (T425lpxr, Chroma), and reflective neutral density filters (Edmund Optics). Quantum catches were derived from the stimulus spectrum [measured using an absolute-irradiance-calibrated spectrometer (USB4000-UV-VIS-ES, Ocean Optics)] and spectral absorbances of mouse rod, cone, and melanopsin pigments (Berson et al., 2002; Govardovskii et al., 2000). Quantum catches were similar among rods, cones, and melanopsin, independently of cones' relative expression of S- and M-cone pigments (Chang et al., 2013; Szel et al., 1992).

To study the cells' ability to encode light intensity, we used bright circular spots on a dark background (diameter=200 μm, Michelson contrast=0.95, stimulus duration=30 sec, inter-stimulus duration=15 sec, 6 repetitions) at 5 intensities at the plane of the photoreceptors (9.4-11.9 log photons cm^{-2} s^{-1}). To allow adaptation of the photoreceptors to the scanning laser, the

data from the first repetition out of 6 in each trial was excluded from analysis. To study the cells' ability to encode decrements in light intensity, we used dark circular spots of five intensities (6-10.4 log photons cm^{-2} s^{-1}) on a bright background (12.5 log photons cm^{-2} s^{-1}). Whereas, to study the glutamate release across the entire field in response to light decrements, we used dark circular spots of five intensities (5.5-9.9 log photons cm^{-2} s^{-1}) on a bright background (11.9 log photons cm^{-2} s^{-1}). To assess directional tuning, we used a sinusoidal grating spanning two spatial periods (spatial frequency=0.132 cycle/degree, Michelson contrast=0.95, stimulus duration=3.65 sec, inter-stimulus duration=5 sec at uniform mean grating intensity) drifted in 8 randomized directions (45° interval, drift speed=4.5 degree/sec, 4 repetitions). Frames of the stimulus movie appeared for 50 µs during the short 185 µs interval between successive sweeps of the imaging laser; thus, no stimulus was presented during the interval of laser scanning and associated imaging (300 µs/sweep). The rapid stimulus flicker (>2000 Hz) was well above critical fusion frequency in mice (Dai et al., 2015).

Patch recording and dye filling of ganglion cells

Whole-cell patch-clamp for current- and voltage-clamp recordings in flat-mount retinas was performed as described (Sabbah et al., 2017b), using a Multiclamp 700B amplifier, Digidata 1550 digitizer, and pClamp 10.5 data acquisition software (Molecular Devices; 10 kHz sampling). Pipettes pulled from thick-walled borosilicate capillaries (P-97; Sutter Instruments) had tip resistances of 5–6 MΩ when filled (in mM, for current-clamp: 120 K-gluconate, 5 NaCl, 4 KCl, 2 EGTA, 10 HEPES, 4 ATP-Mg, 7 phosphocreatine-Tris, 0.3 GTP-Tris, pH 7.3, 270–280 mOsm, and for voltage-clamp: 120 Cs-methanesulfonate, 5 NaCl, 4 CsCl, 2 EGTA, 10 HEPES, 4 ATP-mg, 7 Phosphocreatine-tris, and 0.3 GTP-tris, pH 7.3, 270–280 mOsm). Red fluorescent dye (Alexa Fluor 568; Invitrogen) was added to the pipette for visual guidance under two-photon imaging.

Analysis of glutamate imaging and electrophysiological data

Dendritic glutamate responses were analyzed from time-series images using FluoAnalyzer (Borghuis et al., 2013) and custom Matlab scripts (Sabbah et al., 2017b). To estimate glutamate release at different depths across the IPL, the whole field (84 x 42 µm) was taken as the region of interest (ROI). Whereas, to estimate the glutamate release onto dendrites of a particular RGC, we

patched-filled the RGC with a red fluorescent dye, and imaged those fields that included dendrites showing both red (filled cells) and green (iGluSnFR) fluorescence. To identify synapses on targeted dendrites, we scanned the dendrites for areas where the fluorescence's standard deviation over a time series of iGluSnFR responses was high. These appeared as hot spots on dendrites, which were then manually selected as ROIs (7-10 ROIs per imaged field).

The space-averaged pixel intensity within such ROIs was the activity readout for the associated cell, a proxy for its spike rate (Sabbah et al., 2017c). Fluorescence responses are reported as normalized increases as follows:

$$\frac{\Delta F}{F} = \frac{F - F_0}{F_0}, \quad (1)$$

where F denotes instantaneous fluorescence and F_0 mean fluorescence over a 1-sec period immediately preceding stimulus onset. Intensity-Response (IR) curves were calculated using the steady-state response, taken as the last 5 sec of the 30-sec light-evoked response. The ability of cells to report the intensity of light was assessed by fitting the sigmoidal Naka-Rashton function (Naka and Rushton, 1966) to the cell's steady state response to various stimulus intensities (R):

$$R = R_{\max} * 10^{(nE)} / (10^{(nE)} + 10^{(nK)}), \quad (2)$$

where $R_{\max}$ stands for the cell's predicted maximum response, n for the slope of the function, E for the light intensity measured in units of log photons cm^{-2} s^{-1}, and K represents the cell's sensitivity.

The magnitude of steady state glutamate release was calculated as the difference between the maximum and minimum glutamate release across the five stimulus intensities tested. This magnitude is influenced by the permanence of the response and by the capacity of glutamate release to encode light intensity. Magnitude of zero indicates no variation in the steady state response across stimulus intensities, whether because glutamate release is transient or because it

is sustained but not correlated with intensity. To quantify the sustained glutamate release in relative terms, we developed the following persistence index:

$$Per = \begin{cases} 1 + \frac{G_1 - G_0}{\max(|G_1|, |G_0|)}, G_0 > 0 \\ 1 - \frac{G_1 - G_0}{\max(|G_1|, |G_0|)}, G_0 \leq 0 \end{cases}, \quad (3)$$

where G_0 and G_1 are, respectively, the average glutamate release over the first and last 5 sec of the highest-intensity stimulus. The persistence index ranges from 0 (the glutamate signal returned the baseline by the end of the stimulus, a transient response) to 1 (the glutamate signal remained constant throughout the stimulus duration, a sustained response).

The sensitivity of glutamate release was derived by fitting a third-order polynomial to the IR curve and interpolating a threshold intensity corresponding to a fixed response criterion. Sensitivity was defined as the reciprocal of this threshold intensity (Sabbah et al., 2013). The response criterion was set to a value low enough (0.022 $\Delta F/F$) to be represented in IR curves across the whole IPL. For excitatory currents recordings, we used a response criterion of 10 pA. The dynamic range of steady-state responses was calculated as the 10^{th} and 90^{th} percentiles of the first derivative of the fitted Naka-Rashton function. However, the function did not reach saturation at 85% IPL depth, deeming the estimate unreliable and causing its exclusion. For all stimuli tested, the response amplitude represented the normalized fluorescence increases (for glutamate imaging), average firing rate (for current-clamp recording under control conditions), average lower envelope of the voltage response (for current-clamp recording under any pharmacological manipulation), or average current response (for voltage-clamp recording under any condition). All data were analyzed using custom Matlab scripts.

To evaluate the glutamate release onto individual RGC dendrites at the ON-OFF transition zone, we selected ~150 ROIs from the fluorescence time series acquired in response to the stimuli of the highest intensity. ROIs were classified as either dominated by an ON or OFF response based on whether the mean response during the stimulus' light phase was higher ('ON ROIs') or lower ('OFF ROIs') than that during the stimulus' dark phase. Thereafter, the mean response of ON and OFF ROIs was calculated. This procedure was repeated for several IPL depth profiles.

The preferred direction of a cell was estimated as the angle of the vector sum following[35]:

$$\mathrm{PD} = \arg \sum_{\varphi} r(\varphi) e^{i\varphi}, \quad (4)$$

where r is the response amplitude to stimuli moving at direction φ (0, 45,…,315). The direction selectivity index (DSI) of cells which may range between 0 (no direction selectivity) and 1 (highest direction selectivity) was calculated as:

$$\mathrm{DSI} = \left| \sum_{\varphi} r(\varphi) \mathrm{e}^{i\varphi} \right| \Big/ \sum_{\varphi} r(\varphi). \quad (5)$$

The response amplitude r represented the average response from the stimulus onset to 2 sec following stimulus termination, to capture the OFF responses.

Immunohistochemistry of retina and brain

After recording, retinas were fixed (4% paraformaldehyde, 30 min, 20°C) and counterstained with one or more antibodies: 1. guinea pig anti-Rbpms (1:1000, RNA-binding protein with multiple splicing; 1832-Rbpms, PhosphoSolutions), a pan-ganglion-cell marker) (Kwong et al., 2011); 2. goat anti-ChAT (1:100, anti-choline acetyltransferase; AB144P, Millipore); 3. rabbit anti-melanopsin (1:1000, Advanced Targeting Systems); or 4. chicken anti-GFP (1:1000, ab13970 Abcam), to enhance the fluorescence of the GFP-based GCaMP6f indicator.

Serial electron microscopic reconstruction of retinal neurons

Tissue preparation and EM acquisition were performed as previously described (Ding et al., 2016). A retina (k0725) from an adult wild-type mouse (C57BL/6; postnatal day 30) was stained for EM while preserving the intracellular structure and details. A retinal block face of ~200x400 µm was imaged using a serial block-face scanning EM system (the incident electron beam was of 2.0 keV, ~110 pA). Images were acquired with a pixel dwell time of 2.5 µs and size of 13.2×13.2 nm. The section thickness was set to 26 nm. Imaging of 10,112 consecutive block faces resulted in aligned data volumes of 4,992×16,000×10,112 voxels, comprising a spatial volume of

~50×210×260 μm^3. The imaged region spanned the IPL with parts of the GCL and INL. The data set was split into cubes (128×128×128 voxels) for viewing in webKnossos (https://webknossos.org/). The skeletons of cells were manually traced using the KNOSSOS annotation platform. Skeletons were annotated by placing nodes in the relative center of a neurite's section, branch points, and somas. All skeletons were traced by at least two observers and any discrepancies resolved to ensure accuracy. We assigned BC to established categories (Helmstaedter et al., 2013; Kim et al., 2014; Wassle et al., 2009) based on stratification level and lateral dimensions of the axonal arbor. For densely sampled neighboring BCs, the tiling pattern of arbors further aided the assignment to types.

For each BC, we calculated neurites density as a function of IPL depth, where IPL depth=0% represents the INL-IPL boundary, and 100% represents the IPL-GCL boundary. The 5^{th} percentile neurite density of the axon terminal of all type 2 BCs marked the INL-IPL boundary, whereas the 95^{th} percentile neurite density of the axon terminal of all rod BCs marked the IPL-GCL boundary. The slight tilt of the retinal laminae relative to the cutting plane was accounted for when calculating the IPL depth of cells. All analyses on skeleton data were performed using MATLAB. Morphological statistics of EM-traced cells were compared to those of traces obtained from light microscopy (LM) data. EM traces of the dendritic arbors of several RGCs and were incomplete due to the small size of the EM volume. Thus, we prioritized morphological parameters that are least susceptible to the incompleteness of traces: the stratification pattern, soma diameter, and branch point density.

Statistical analysis

Permutation one-way ANOVA was used for testing the effect of transmission stage (glutamate release, excitatory currents, and firing rate) on the persistence and magnitude of responses. A permutation t-test was used for comparing responses' persistence and magnitude between M4 ipRGCs and conventional ON-DSGCs. As data often deviated from assumptions of normality (Kolmogorov Smirnov test) and homoscedasticity (Bartlett's test), we utilized appropriate permutation tests with a significance level of 0.05. All analyses were performed in the R statistical software.

References

An, K., Zhao, H., Miao, Y., Xu, Q., Li, Y.F., Ma, Y.Q., Shi, Y.M., Shen, J.W., Meng, J.J., Yao, Y.G., *et al.* (2020). A circadian rhythm-gated subcortical pathway for nighttime-light-induced depressive-like behaviors in mice. Nature Neuroscience 23, 869-880.

Awatramani, G.B., and Slaughter, M.M. (2000). Origin of transient and sustained responses in ganglion cells of the retina. Journal of Neuroscience 20, 7087-7095.

Baden, T., Berens, P., Bethge, M., and Euler, T. (2013). Spikes in mammalian bipolar cells support temporal layering of the inner retina. Curr Biol 23, 48-52.

Baden, T., Berens, P., Franke, K., Román Rosón, M., Bethge, M., and Euler, T. (2016). The functional diversity of retinal ganglion cells in the mouse. Nature 529, 345-350.

Baver, S.B., Pickard, G.E., Sollars, P.J., and Pickard, G.E. (2008). Two types of melanopsin retinal ganglion cell differentially innervate the hypothalamic suprachiasmatic nucleus and the olivary pretectal nucleus. Eur J Neurosci 27, 1763-1770.

Berson, D.M., Dunn, F.A., and Takao, M. (2002). Phototransduction by retinal ganglion cells that set the circadian clock. Science 295, 1070-1073.

Blanco, R., Vaquero, C.F., and DelaVilla, P. (1996). The effects of GABA and glycine on horizontal cells of the rabbit retina. Vision Research 36, 3987-3995.

Borghuis, B.G., Marvin, J.S., Looger, L.L., and Demb, J.B. (2013). Two-photon imaging of nonlinear glutamate release dynamics at bipolar cell synapses in the mouse retina. Journal of Neuroscience 33, 10972-10985.

Chang, L., Breuninger, T., and Euler, T. (2013). Chromatic coding from cone-type unselective circuits in the mouse retina. Neuron 77, 559-571.

Chen, S.K., Badea, T.C., and Hattar, S. (2011). Photoentrainment and pupillary light reflex are mediated by distinct populations of ipRGCs. Nature 476, 92-95.

Dai, X., Zhang, H., He, Y., Qi, Y., Chang, B., and Pang, J.-j. (2015). The frequency-response electroretinogram distinguishes cone and abnormal rod function in rd12 mice. PLoS One 10, e0117570.

Della Santina, L., Kuo, S.P., Yoshimatsu, T., Okawa, H., Suzuki, S.C., Hoon, M., Tsuboyama, K., Rieke, F., and Wong, R.O. (2016). Glutamatergic monopolar interneurons provide a novel pathway of excitation in the mouse retina. Curr Biol 26, 2070-2077.

DeVries, S.H., Li, W., and Saszik, S. (2006). Parallel processing in two transmitter microenvironments at the cone photoreceptor synapse. Neuron 50, 735-748.

Ding, H., Smith, R.G., Poleg-Polsky, A., Diamond, J.S., and Briggman, K.L. (2016). Species-specific wiring for direction selectivity in the mammalian retina. Nature 535, 105-110.

Dowling, J.E. (1968). Synaptic organization of the frog retina: an electron microscopic analysis comparing the retinas of frogs and primates. Proc R Soc Lond B Biol Sci 170, 205-228.

Dowling, J.E. (1987). The retina: an approachable part of the brain (Cambridge, MA: Harvard University Press).

Dumitrescu, O.N., Pucci, F.G., Wong, K.Y., and Berson, D.M. (2009). Ectopic retinal ON bipolar cell synapses in the OFF inner plexiform layer: contacts with dopaminergic amacrine cells and melanopsin ganglion cells. J Comp Neurol 517, 226-244.

Ecker, J.L., Dumitrescu, O.N., Wong, K.Y., Alam, N.M., Chen, S.-K., LeGates, T., Renna, J.M., Prusky, G.T., Berson, D.M., and Hattar, S. (2010). Melanopsin-expressing retinal ganglion-cell photoreceptors: cellular diversity and role in pattern vision. Neuron 67, 49-60.

Fernandez, D.C., Fogerson, P.M., Ospri, L.L., Layne, R.M., Akasako, M., Singer, J.H., Berson, D.M., and Hattar, S. (2018). Light affects mood and learning through distinct retina-brain pathways. Cell 175, 71-84.

Franke, K., Berens, P., Schubert, T., Bethge, M., Euler, T., and Baden, T. (2017). Inhibition decorrelates visual feature representations in the inner retina. Nature 542, 439-444.

Govardovskii, V.I., Fyhrquist, N., Reuter, T., Kuzmin, D.G., and Donner, K. (2000). In search of the visual pigment template. Visual Neuroscience 17, 509-528.

Greferath, U., Grunert, U., Fritschy, J.M., Stephenson, A., Mohler, H., and Wassle, H. (1995). Gaba A receptor subunits have differential distributions in the rat retina - in-situ hybridization and immunohistochemistry. J Comp Neurol 353, 553-571.

Greferath, U., Grunert, U., Muller, F., and Wassle, H. (1994). Localization of GABAA receptors in the rabbit retina. Cell Tissue Res 276, 295-307.

Helmstaedter, M., Briggman, K.L., Turaga, S.C., Jain, V., Seung, H.S., and Denk, W. (2013). Connectomic reconstruction of the inner plexiform layer in the mouse retina. Nature 500, 168-174.

Higgs, M.H., and Lukasiewicz, P.D. (1999). Glutamate uptake limits synaptic excitation of retinal ganglion cells. Journal of Neuroscience 19, 3691-3700.

Hoshi, H., Liu, W.L., Massey, S.C., and Mills, S.L. (2009). ON inputs to the OFF layer: bipolar cells that break the stratification rules of the retina. Journal of Neuroscience 29, 8875-8883.

Hughes, T.E., Grunert, U., and Karten, H.J. (1991). GABAA receptors in the retina of the cat: an immunohistochemical study of wholemounts, sections, and dissociated cells. Vis Neurosci 6, 229-238.

Ivanova, E., Toychiev, A.H., Yee, C.W., and Sagdullaev, B.T. (2013). Optimized protocol for retinal wholemount preparation for imaging and immunohistochemistry. J Vis Exp, e51018.

Kim, H.L., Jeon, J.H., Koo, T.H., Lee, U.Y., Jeong, E., Chun, M.H., Moon, J.I., Massey, S.C., and Kim, I.B. (2012). Axonal synapses utilize multiple synaptic ribbons in the mammalian retina. PLoS One 7, e52295.

Kim, J.S., Greene, M.J., Zlateski, A., Lee, K., Richardson, M., Turaga, S.C., Purcaro, M., Balkam, M., Robinson, A., Behabadi, B.F., *et al.* (2014). Space-time wiring specificity supports direction selectivity in the retina. Nature 509, 331-336.

Kim, T., Soto, F., and Kerschensteiner, D. (2015). An excitatory amacrine cell detects object motion and provides feature-selective input to ganglion cells in the mouse retina. Elife 4.

Kwong, J.M.K., Quan, A., Kyung, H., Piri, N., and Caprioli, J. (2011). Quantitative analysis of retinal ganglion cell survival with rbpms immunolabeling in animal models of optic neuropathies. Invest Ophthalmol Vis Sci 52, 9694-9702.

LeGates, T.A., Altimus, C.M., Wang, H., Lee, H.K., Yang, S.G., Zhao, H.Q., Kirkwood, A., Weber, E.T., and Hattar, S. (2012). Aberrant light directly impairs mood and learning through melanopsin-expressing neurons. Nature 491, 594-598.

Lilley, B.N., Sabbah, S., Hunyara, J.L., Gribble, K.D., Al-Khindi, T., Xiong, J., Wu, Z., Berson, D.M., and Kolodkin, A.L. (2019). Genetic access to neurons in the accessory optic system reveals a role for Sema6A in midbrain circuitry mediating motion perception. J Comp Neurol.

Lucas, R.J., Hattar, S., Takao, M., Berson, D.M., Foster, R.G., and Yau, K.W. (2003). Diminished pupillary light reflex at high irradiances in melanopsin-knockout mice. Science 299, 245-247.

Marvin, J.S., Borghuis, B.G., Tian, L., Cichon, J., Harnett, M.T., Akerboom, J., Gordus, A., Renninger, S.L., Chen, T.-W., Bargmann, C.I., *et al.* (2013). An optimized fluorescent probe for visualizing glutamate neurotransmission. Nature Methods 10, 162-170.

Naka, K.I., and Rushton, W.A. (1966). S-potentials from luminosity units in the retina of fish (Cyprinidae). J Physiol 185, 587-599.

Park, S.J.H., Lieberman, E.E., Ke, J.-B., Rho, N., Ghorbani, P., Rahmani, P., Jun, N.Y., Lee, H.-L., Kim, I.-J., Briggman, K.L., *et al.* (2020). Connectomic analysis reveals an interneuron with an integral role in the retinal circuit for night vision. eLife 9, e56077.

Provencio, I., Rodriguez, I.R., Jiang, G.S., Hayes, W.P., Moreira, E.F., and Rollag, M.D. (2000). A novel human opsin in the inner retina. Journal of Neuroscience 20, 600-605.

Quattrochi, L.E., Stabio, M.E., Kim, I., Ilardi, M.C., Michelle Fogerson, P., Leyrer, M.L., and Berson, D.M. (2019). The M6 cell: A small-field bistratified photosensitive retinal ganglion cell. J Comp Neurol 527, 297-311.

Reifler, A.N., Chervenak, A.P., Dolikian, M.E., Benenati, B.A., Li, B.Y., Wachter, R.D., Lynch, A.M., Demertzis, Z.D., Meyers, B.S., Abufarha, F.S., *et al.* (2015). All spiking, sustained ON displaced amacrine cells receive gap-junction input from melanopsin ganglion cells. Curr Biol 25, 2878-2878.

Roska, B., and Werblin, F. (2001). Vertical interactions across ten parallel, stacked representations in the mammalian retina. Nature 410, 583-587.

Sabbah, S., Berg, D., Papendorp, C., Briggman, K.L., and Berson, D.M. (2017a). A Cre mouse line for probing irradiance- and direction-encoding retinal networks. eneuro.

Sabbah, S., Berg, D., Papendorp, C., Briggman, K.L., and Berson, D.M. (2017b). A Cre mouse line for probing irradiance- and direction-encoding retinal networks. eNeuro 4.

Sabbah, S., Gemmer, J.A., Bhatia-Lin, A., Manoff, G., Castro, G., Siegel, J.K., Jeffery, N., and Berson, D.M. (2017c). A retinal code for motion along the gravitational and body axes. Nature 546, 492-497.

Sabbah, S., Habib-Nayany, M.F., Dargaei, Z., Hauser, F.E., Kamermans, M., and Hawryshyn, C.W. (2013). Retinal region of polarization sensitivity switches during ontogeny of rainbow trout. J Neurosci 33, 7428-7438.

Schmidt, T.M., Alam, N.M., Chen, S., Kofuji, P., Li, W., Prusky, G.T., and Hattar, S. (2014). A role for melanopsin in alpha retinal ganglion cells and contrast detection. Neuron 82, 781-788.

Schmidt, T.M., and Kofuji, P. (2009). Functional and morphological differences among intrinsically photosensitive retinal ganglion cells. Journal of Neuroscience 29, 476-482.

Schmidt, T.M., and Kofuji, P. (2011). Structure and function of bistratified intrinsically photosensitive retinal ganglion cells in the mouse. J Comp Neurol 519, 1492-1504.

Shekhar, K., Lapan, S.W., Whitney, I.E., Tran, N.M., Macosko, E.Z., Kowalczyk, M., Adiconis, X., Levin, J.Z., Nemesh, J., Goldman, M.*, et al.* (2016). Comprehensive classification of retinal bipolar neurons by single-cell transcriptomics. Cell 166, 1308-1323 e1330.

Szel, A., Rohlich, P., Caffe, A.R., Juliusson, B., Aguirre, G., and Vanveen, T. (1992). Unique topographic separation of 2 spectral classes of cones in the mouse retina. J Comp Neurol 325, 327-342.

Vardi, N., Masarachia, P., and Sterling, P. (1992). Immunoreactivity to GABAA receptor in the outer plexiform layer of the cat retina. J Comp Neurol 320, 394-397.

Wassle, H., Koulen, P., Brandstatter, J.H., Fletcher, E.L., and Becker, C.M. (1998). Glycine and GABA receptors in the mammalian retina. Vision Research 38, 1411-1430.

Wassle, H., Puller, C., Muller, F., and Haverkamp, S. (2009). Cone contacts, mosaics, and territories of bipolar cells in the mouse retina. Journal of Neuroscience 29, 106-117.

Wong, K.Y. (2012). A retinal ganglion cell that can signal irradiance continuously for 10 hours. Journal of Neuroscience 32, 11478-11485.

Wong, K.Y., Dunn, F.A., Graham, D.M., and Berson, D.M. (2007). Synaptic influences on rat ganglion-cell photoreceptors. J Physiol (Lond) 582, 279-296.

Wu, S.M., Gao, F., and Maple, B.R. (2000). Functional architecture of synapses in the inner retina: Segregation of visual signals by stratification of bipolar cell axon terminals. Journal of Neuroscience 20, 4462-4470.

Zhang, D.Q., Wong, K.Y., Sollars, P.J., Berson, D.M., Pickard, G.E., and McMahon, D.G. (2008). Intraretinal signaling by ganglion cell photoreceptors to dopaminergic amacrine neurons. Proc Natl Acad Sci USA 105, 14181-14186.

Zhao, X., Reifler, A.N., Schroeder, M.M., Jaeckel, E.R., Chervenak, A.P., and Wong, K.Y. (2017). Mechanisms creating transient and sustained photoresponses in mammalian retinal ganglion cells. Journal of General Physiology 149, 335-353.

Zhao, X.W., Stafford, B.K., Godin, A.L., King, W.M., and Wong, K.Y. (2014). Photoresponse diversity among the five types of intrinsically photosensitive retinal ganglion cells. J Physiol (Lond) 592, 1619-1636.